

REVIEW

New trends in biophotonics

László Fábrián, Anna Mathesz, András Dér*

Institute of Biophysics, Biological Research Centre of the Hungarian Academy of Sciences, Szeged, Hungary

ABSTRACT Photonic structures offer a promising alternative of conventional electronic ones, especially for future information technological applications. Instead of conductors and transistors, their optical analogues (miniature light guides and optical switches, respectively) are serving as passive and active elements processing information in photonic circuits. One of the biggest challenges in this respect is to find proper nonlinear optical (NLO) materials that are able to actively control the flow of information in integrated optical (IO) circuits. Several inorganic and organic materials have been considered for this special application, requiring high speed, sensitivity, reliability and long-term stability. So far, however, none of them is regarded as the optimal solution. In 2002, we suggested an especially stable, light-sensitive biomaterial, the protein bacteriorhodopsin (bR), to be used as an active material in NLO structures of IO applications (Ormos et al. 2002). An IO switching and modulation using a bR adlayer on a grating-coupled planar optical waveguide was also demonstrated. This publication inspired a number of upcoming research papers dealing with the application of bR in different optical switch structures, defining a new trend in photonics, using hybride structures comprised of passive inorganic, and active biomaterials. Below, we give a brief overview of the relevant, recent results.

Acta Biol Szeged 59(Suppl.2):189-202 (2015)

KEY WORDS

all-optical switching
bacteriorhodopsin
biophotonics
integrated optics
optical logic gates

Introduction

Time will come when the continuously growing internet traffic and the high demand for faster data processing applications cannot be fulfilled by present, state-of-the-art electronic devices. Modern electronic circuits require more and more components (*e.g.*, transistors) to be integrated on a small silicon chip, but the minimal size of these electronic elements is limited.

In 1965, director of R&D Laboratories at Fairchild Semiconductor, Gordon E. Moore made a prediction about the future of integrated electronics. His finding (named after him Moore's Law) was that the number of electronic components integrated on a silicon wafer of unit area is doubling in every 18 month (Moore 1965). This predicted exponential growth has been valid for a long time, but experts say that this trend cannot be sustained for a long time: "Moore's Law will soon hit the wall".

Nowadays, integrated electronic components are fabricated by chemical, physical or electrochemical vapor deposition (CVD, PVD, ECD) methods, molecular beam epitaxy (MBE) and recently, atomic layer deposition (ALD). It is clear, that the size of integrated electronic components

cannot be decreased below a limit that will be reached soon. The most important problems of today's microelectronic devices are, among others, electromagnetic interference and heat dissipation. Hence, although microelectronics will have the leading role in everyday's telecommunication and data processing applications, several alternative solutions are also intensively researched to keep up with the increasing demands of information technology. One of the most promising approaches is the field of integrated optics (IO), which provides micro-devices operating by light pulses as information carriers, at wavelengths typically in the visible and near-infrared spectrum.

IO is a rapidly emerging discipline of engineering optics aiming at integrating miniature photonic devices on a common substrate. One of the most important areas of applications in integrated optics is telecommunication, where all-optical data processing is the most promising direction. Unlike microelectronic integration, where silicon is the dominant material, photonic integrated circuits are fabricated also from *e.g.*, electro-optic crystals, various polymers and semiconductor materials. State-of-the-art photonic integration technology can provide the passive elements of optical integrated circuits, based either on silicon, glass or plastic materials. As the technologies are readily developed, the most challenging task of integrated optical research is to find the most suitable materials with appropriate nonlinear optical (NLO) properties that can serve as active elements in inte-

Submitted Apr 23, 2015; Accepted July 27, 2015

*Corresponding author. E-mail: der.andras@brc.mta.hu

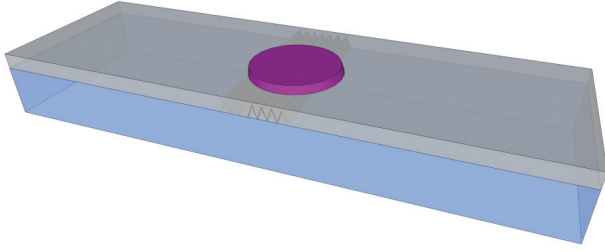


Figure 1. Schematic representation of the slab waveguide with a dried purple membrane patch above the grating coupler.

grated optical circuits. According to recent views, the versatile and cost-effective organic materials represent a promising alternative of the currently used semiconductor materials, to be the basis of active IO elements (Haque and Nelson 2010). So far, specifically designed organic, pi-conjugated molecular materials have attracted the most interest (Service 1995; Hu et al. 2008; Hales et al. 2010), but their applicability in IO is still to be verified.

The simplest passive element of an integrated optical circuit is a waveguide which is the optical analog of electrical wires. Since guided modes of an optical waveguide have important role in photonic devices, in the next sections we present the calculation of their characteristic parameters as well as an experimental method which will also be the basis of a biophotonic switching device.

Guided modes in a slab waveguide

Optical waveguides are the most important passive components of an integrated optical circuit. Their common feature is a high refractive index core in which the light wave propagates by total internal reflection at the boundaries. Although they exist in many forms (*e.g.*, ridge, channel, etc.) suited for the application in question, their light-guiding properties are very similar, and can be studied – in some basic cases – analytically. To demonstrate the analytical method and discover the most important properties of guided waves, here we deal with the simplest waveguide form, the so-called *slab waveguide*. For the description of waveguiding and the guided modes, we will use Maxwell's equations, and we presume that the reader is familiar with the basic operations of vector analysis.

The *guiding layer* of the slab waveguide is a thin (~200 nm) dielectric layer of high refractive index, evaporated on a glass, polymer or plastic *substrate* (Fig. 1). There is also a third layer (the so-called *adlayer*) on the top of the guiding layer which later will have an important role in biophotonic applications. Therefore, the waveguide theory presented below is called the theory of three-layer waveguides. The validity of this theory will also be discussed at the end of this section.

Waveguiding occurs via total internal reflections at the substrate-film and film-adlayer interfaces. Incident elementary light beams reflected from the two interfaces interfere with each other, and the resulting interference pattern determines the cross-sectional intensity distribution of the *guided mode*. Since the light propagating in the guiding layer is an electromagnetic wave, the exact description of the phenomenon can be done using Maxwell's equations. We consider non-conducting dielectric layers without free charges and free currents. In this case, Maxwell's equations reduce themselves to the following:

$$\nabla \cdot \vec{E} = 0$$

$$\mu_0(\nabla \cdot \vec{H}) = 0$$

$$\nabla \times \vec{E} = -\mu_0 \frac{\partial \vec{H}}{\partial t}$$

$$\nabla \times \vec{H} = \epsilon_0 \epsilon \frac{\partial \vec{E}}{\partial t}$$

where \vec{E} and \vec{H} are the electric and magnetic field vectors of the electromagnetic wave, ϵ_0 is the absolute permittivity of the vacuum, ϵ is the relative permittivity of the material and μ_0 is the vacuum permeability. From the above equations, we can compose the *wave equations* corresponding to both the electric and the magnetic field vectors:

$$\nabla^2 \vec{E} - \frac{n^2}{c^2} \frac{\partial^2 \vec{E}}{\partial t^2} = 0$$

$$\nabla^2 \vec{H} - \frac{n^2}{c^2} \frac{\partial^2 \vec{H}}{\partial t^2} = 0$$

where c is the speed of light in vacuum, 3×10^8 m/s, and n is the refractive index of the material in which the wave is propagating.

Furthermore, we also consider a semi-infinite substrate and adlayer with refractive indices n_s and n_a , respectively, between them a guiding layer of refractive index n_f and thickness d_f . Since the media considered here are isotropic, the y -dependence of the fields is zero, which is expressed by the spatial operator $\partial/\partial y = 0$, when applied to the \vec{E} and \vec{H} vectors. Therefore, the electric and magnetic fields of a monochromatic plane wave with an angular frequency of ω which obey the above restrictions, can be written in the form:

$$\vec{E}(\vec{r}, t) = \vec{E}_0(x) \exp[-i(\omega t - \beta z)]$$

$$\vec{H}(\vec{r}, t) = \vec{H}_0(x) \exp[-i(\omega t - \beta z)]$$

where β is the component of the wave vector parallel to the z -axis, the so-called *propagation constant*. Guided

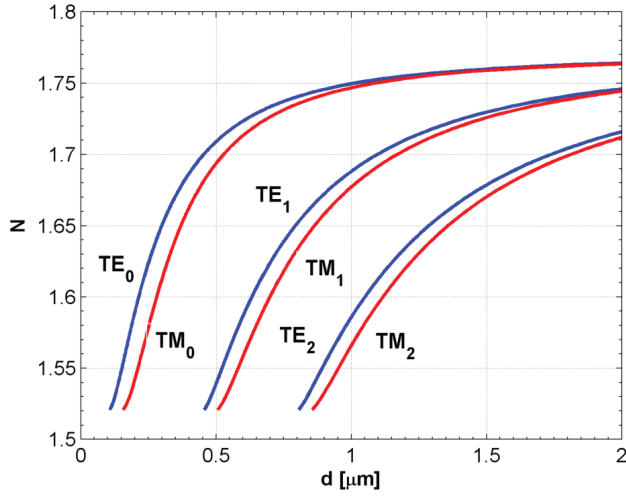


Figure 2. Calculated effective refractive indices of different guided modes in the function of the guiding layer thickness. Waveguide parameters: $n_s = 1.52$, $n_f = 1.77$, $n_A = 1n$, $\lambda = 632.8$ nm.

modes are tightly confined in the guiding layer, therefore, we look for plane wave solutions that are harmonic in the guiding layer and exponentially decaying in the substrate and adlayer. Substituting the plane wave solutions into the wave equations, one can get two distinct solutions which depend on the polarization of the incident light. When the polarization direction of the wave is parallel to the plane of incidence (e.g., *p*-polarized), the mode is called a TM (*transversal magnetic*) mode, when it is perpendicular to the plane of incidence, the mode is a TE (*transversal electric*) mode. After some basic algebraic operations, one can get the *mode equations* corresponding to the *m*th TE and TM guided modes, respectively:

$$k_0 d_F \sqrt{n_F^2 - N_{TE}^2} = \arctan \left[\frac{\sqrt{N_{TE}^2 - n_s^2}}{\sqrt{n_F^2 - N_{TE}^2}} \right] + \arctan \left[\frac{\sqrt{N_{TE}^2 - n_A^2}}{\sqrt{n_F^2 - N_{TE}^2}} \right] + m\pi$$

$$k_0 d_F \sqrt{n_F^2 - N_{TM}^2} = \arctan \left[\frac{n_F^2 \sqrt{N_{TM}^2 - n_s^2}}{n_s^2 \sqrt{n_F^2 - N_{TM}^2}} \right] + \arctan \left[\frac{n_F^2 \sqrt{N_{TM}^2 - n_A^2}}{n_A^2 \sqrt{n_F^2 - N_{TM}^2}} \right] + m\pi$$

where k_0 is the vacuum wavenumber of the monochromatic light, N_i ($i=TE, TM$) are the so-called *effective refractive indices* of the modes, defined by $N = \beta/k_0$. The $\arctan(\dots)$ terms in the above equations represent the Goos – Hänchen shifts, the phase shifts of the wave upon total internal reflections on the boundaries. The effective refractive index of a guided mode depends upon the wavelength and the waveguide parameters, namely, the refractive indices of the three layers and the thickness of the guiding layer. Solutions of the mode equations give the effective refractive index of a given mode,

from which the cross sectional light intensity distribution can also be calculated.

The effective indices of some guided modes as the function of the guiding layer thickness are shown on Figure 2. It can be clearly seen that the TE and TM modes are unambiguously separated by the waveguide each having a distinct effective index. From geometric considerations, it can be shown that the effective refractive index of a guided mode always lies between the refractive index of the substrate and the guiding layer. Zeroth TE mode has always the highest effective index, close to the refractive index of the guiding layer. If we have a waveguide in which only the zeroth mode(s) can propagate, it is called a *single mode* waveguide.

Two other important properties of a slab waveguide are the *cut-off wavelength* and the *cut-off thickness*. For a given thickness and waveguide refractive indices, the former determines the maximal wavelength of the monochromatic wave that can propagate in the guiding layer as a guided mode. The latter, assuming that the wavelength and the refractive indices are given, tells us about the minimal thickness of the guiding layer in which a guided mode can propagate. The cut-off wavelengths of the zeroth modes is defined by

$$\lambda_c = 2\pi d_F \frac{\sqrt{n_F^2 - n_s^2}}{\arctan \left[\left(\frac{n_F^2}{n_A^2} \right)^\alpha \frac{n_s^2 - n_A^2}{\sqrt{n_F^2 - n_s^2}} \right]}$$

where $\alpha = 0, 1$ corresponds to the TE and TM modes, respectively. The cut-off thickness of the *m*th mode of a slab waveguide is given by

$$d_c = \frac{\lambda_0}{2\pi} \frac{\arctan \left[\left(\frac{n_F^2}{n_A^2} \right)^\alpha \frac{n_s^2 - n_A^2}{\sqrt{n_F^2 - n_s^2}} \right] + m\pi}{\sqrt{n_F^2 - n_s^2}}$$

where, again, $\alpha = 0$, corresponds to the TE and TM modes, respectively.

As we have seen, the electric field, consequently, the light intensity outside of the guiding layer, is not zero, and it is decaying exponentially. Since the effective index of the mode also depends both on n_s and n_A , it can be realized as the outlying, decaying part of the confined radiation also “feels” the refractive indices of the substrate and the adlayer. This exponentially decaying part of the guided mode is called the *evanescent wave* which has an important role also in sensory applications (Dér et al. 2010) based on optical waveguides.

The distance measured in the substrate or the adlayer at which the electric field decays to its $1/e$ value (corresponding to the interface boundary) is the so-called *penetration depth*. Any adlayer (or substrate) material that is inside the penetra-

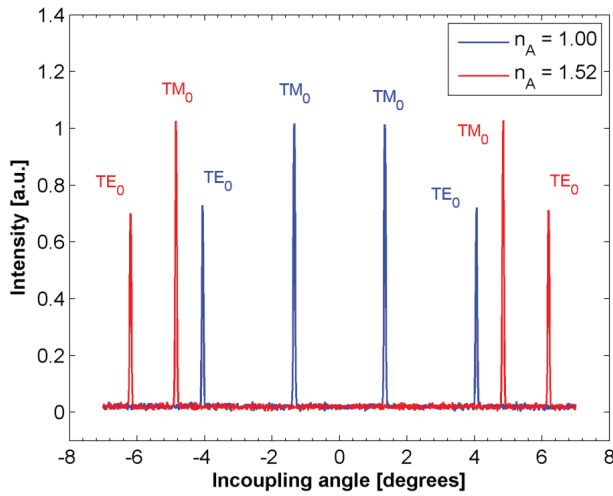


Figure 3. Observed intensity peaks corresponding to the zeroth TM and TE modes in case of $n_A = 1.00$ (blue line) and $n_A = 1.52$ (red line). Guided modes symmetrically located around 0 degrees (normal incidence) were measured by two detectors placed at the ends of the waveguide.

tion depth influences the effective index of a guided mode. The above theory of the three-layer slab waveguides as well as its consequences is valid only in the case when the adlayer and the substrate are thicker than the penetration depth. The penetration depth in each medium is given by:

$$\Delta x_i = \frac{\lambda_0}{2\pi} \frac{1}{\sqrt{N^2 - n_i^2}} \frac{1}{\left[\frac{N^2}{n_p^2} + \frac{N^2}{n_i^2} - 1 \right]^\alpha}$$

where $i=S,A$ corresponding to the substrate and the adlayer and $\alpha = 0,1$ apply to the TE and TM modes, respectively. Usually, the penetration depth is in the order of the wavelength.

Optical Waveguide Lightmode Spectroscopy

As we have seen, a guided mode of the slab waveguide is uniquely characterized by its effective refractive index which depends only on the waveguide parameters and the wavelength of the applied electromagnetic radiation. Until now, we have not emphasized the role and importance of the uppermost layer, the adlayer, which is indicated on Figure 1 as a circular patch. Commercially available slab optical waveguides, in the simplest case, are fabricated by evaporating a thin dielectric layer on a – usually glass or quartz – substrate. Literally, it is only a two-layer waveguide; the third layer in this case is the air above the thin guiding layer. In integrated optical applications using bare waveguides or optical fibers, the adlayer can be any arbitrary material placed (evaporated, dried, etc.) on the top of the guiding layer. Since the effective refractive index of the guided mode depends also on the

refractive index of the adlayer, the guided mode inside the guiding layer can be manipulated by the adlayer. This phenomenon is exploited in sensory and, as we shall see in detail, in waveguide-based photonic applications.

One of the modern experimental methods used for refractive index measurement is based on the measurement of the effective refractive index of guided modes and called *Optical Waveguide Lightmode Spectroscopy* (OWLS). In this section we will introduce the basic technique and later it will be exploited as a possible integrated optical application.

So far, we have investigated a radiation that is confined, propagating in a very thin layer, but have not told how the light can be introduced into the guiding layer. A plain method is the so-called *end-coupling* when we simply direct the monochromatic light into the guiding layer, for example, from an optical fiber. In this case the numerical aperture of the fiber has to be matched with the acceptance angle of the waveguide. This method is rarely used and cannot even be used in case of very thin guiding layers. Another possibility to excite a guided mode is the *prism-coupling*. This method uses evanescent waves occurring at total reflection inside a prism to excite a guided mode in a waveguide which is placed very close (tens of nanometers) to the coupling prism. A third coupling method which is in close connection with the OWLS-technique is discussed in more detail.

Grating couplers are diffraction gratings embedded in the substrate or the guiding layer itself. They can be either amplitude gratings fabricated by sol-gel technique from a master grating, or phase gratings prepared by ion implantation. The impinging beam is diffracted on the grating and the first-order diffracted ray is coupled into the guiding layer. The effective refractive index is only a numerical parameter that characterizes a guided mode unequivocally, but cannot be measured directly. However, several indirect methods exist by which we can measure this parameter. One of them, which will be described in the following, uses a slab waveguide equipped with a grating coupler. Since we usually use single-mode waveguides, in the following the mode order will be taken to be 0 where it is appropriate.

A monochromatic light (e.g., a laser beam) coming from the substrate side of the waveguide is directed onto the grating coupler with an incidence angle of a . The beam will be diffracted into the guiding layer under a diffraction angle determined by the *grating equation*. The waveguide is placed on a rotational stage by which the incident angle of the laser beam can be varied with high precision (typically 10^{-3} deg). Detectors (e.g., photomultiplier tubes, photodiodes) are placed at the ends of the waveguide to measure the intensity of the light propagating in the guiding layer. The intensity signal measured by the detectors can be investigated on an oscilloscope (Fig. 3). When a guided mode is excited, a sharp intensity peak can be observed in the signal of the detector placed in the direction of light propagation, indicating that

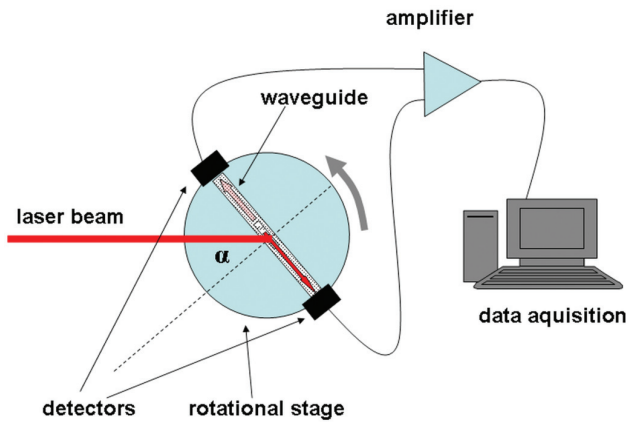


Figure 4. Experimental arrangement of the OWLS-technique used in this work.

the incoupled beam propagates along the waveguide. With this method, angular positions of the peaks corresponding to the guided modes can be precisely measured and the effective mode indices can be calculated by the following formula:

$$N = \sin \alpha + \frac{\lambda}{\Lambda}$$

where α is the incidence angle of the laser corresponding to the measured intensity peak, λ is the wavelength of the monochromatic light and Λ is the grating constant (*e.g.*, the distance between two grooves, in spectroscopy, it is usually given in *lines/mm*). One possible experimental arrangement by which the guided modes can be visualized and investigated is shown on Figure 4.

OWLS is a very sensitive technique for refractive index measurement. Since the parameters (thickness, refractive index) of commercially available slab waveguides are subject to some deviation due to the manufacturing process, they have to be calibrated before use. Calibration is performed in the presence of an adlayer of known refractive index, *e.g.*, in air. When the angular positions of the zeroth TM and TE modes are determined, the two mode equations corresponding to the modes of different polarizations contain only two unknown parameters, namely, the thickness and the refractive index of the guiding layer (assumed that the substrate refractive index is known). The system of mode equations can be solved by numerical methods. Here we must note that the highly nonlinear mode equations require a very accurate determination of angles and numerical solutions of high precision. From the measured incoupling angles the thickness and refractive index of the layer can be calculated.

The waveguides calibrated in this way are ready to be used for refractive index measurements of any material that can be layered on top of the guiding layer. By this method refractive index of liquids, gases and even biological samples

dried from solution can be measured. The OWLS-technique can also be used in sensory applications, like humidity and gas detectors, even the rate of biochemical reactions can be followed by this method.

So far, we have got acquainted with the simplest photonic device which, in many different forms, is the most important passive element of an integrated optical circuit. Even in this simple case, analytical investigation of guided modes requires elaborate mathematical operations. Several analytical methods also exist for somewhat complicated arrangements but usually the analysis of a general-purpose, multilayer waveguide structure uses tricky approximations, and also demands high computational power. A lot of numerical methods are available for integrated optical calculations, and are implemented in complex software packages.

Active components in integrated optical circuits

An integrated optical circuit without active components is like a network of roads without traffic lights. Active elements are necessary to control the propagation of light in a complex optical circuit, like transistors switch currents in electric devices. Control is performed through actuating an active component by some kind of external signal. Nowadays, integrated optical switches and modulators are operated by electric, magnetic, thermal or acoustic energy conversion via a *nonlinear optical* (NLO) material of sufficient properties. Active components based on electro-, or magneto-optic effects change their optical properties upon external voltage or applied magnetic field, while acousto-optic modulators exploit the density change of the material generated by acoustic waves of appropriate frequency. All of these nonlinear optical effects lead to change in the refractive index by which the propagating electromagnetic wave can be altered. Due to size restrictions of this article, a complete review of these methods is impossible.

Bottle-necks of the above methods are the speed and efficiency of the conversion between two forms of energy. Higher-order nonlinear optical coefficients are small, therefore, these active components require high electric or magnetic field to operate which can often lead to the breakdown of the device. Today, integrated electronic switches operate in the nanosecond region.

To overcome the disadvantages of these techniques, *all-optical* methods in which the propagating light is controlled in a purely optical way, are intensively researched. Since the fabrication procedures are very similar to those used to create microelectronic circuits and they are well-developed, bottle-neck of integrated optics is the research of new, efficient materials with appropriate NLO properties that can play the role of active components. Active components of integrated optical circuits can be organic or inorganic crystals, natural or sophisticatedly designed artificial dye molecules (Hales et al. 2010) and even materials of biological origin. There

are several important requirements to be fulfilled by these active materials, like sensitivity, high light-induced refractive index change, mechanical stability, etc. Although biological molecules, especially proteins become unstable when they are extracted from their natural environment, lately, some of them are also being considered for technical use in photonics. Among them, the chromoprotein *bacteriorhodopsin* (bR) has generated the most interest (Song et al. 1994; Vsevolodov 1998; Stuart et al. 2001). Several conceptual optical data-processing applications using bR as active NLO material have also been published (Thoma and Hampp 1994; Zhang et al. 1995; Stuart et al. 2002; Fischer et al. 2003).

Bacteriorhodopsin

Bacteriorhodopsin (bR), a transmembrane proton pumping protein isolated from a fraction of the outer cell membrane (purple membrane, PM) of the salt-loving archaean *Halobacterium salinarum* (Oesterhelt and Stoekenius 1971, 1973; Dér et al. 1995), is the simplest known ion pump and one of the best characterized membrane proteins. Among other retinal-containing proteins – like halorhodopsin, sensory rhodopsin I and II (Stoekenius 1985) –, bR plays an important role in the energetics of the cell. Upon light absorption, bR pumps protons from the cytoplasmic side of the membrane to the extracellular space and the resulting transmembrane proton gradient is used by the ATP synthase for ATP synthesis (Bogomolni et al. 1976; Hartmann et al. 1977). Bacteriorhodopsin is one of the smallest ion pumping membrane proteins, therefore it serves as a model system in the investigation of the structure and functional mechanism of active ion transport processes at the atomic level.

The protein – with a molecular weight of 26 kDa – is consisted of seven α -helices that span the purple membrane with a thickness of about 5 nm. The protein molecules are ordered in a regular two-dimensional hexagonal lattice in PM, in a trimeric form (Henderson and Shotton 1980; Henderson et al. 1986). The amino acid residue sequence was also determined in one of the early studies (Ovchinnikov et al. 1979). The structure and function of the protein (in some details) are very similar to those of the rhodopsin found in the eye (Oesterhelt and Stoekenius 1971). Atomic structure of the protein obtained from X-ray crystallographic experiments is shown on Figure 5. The direction of proton pumping is pointing downward from the cytoplasmic side of the membrane.

The light-adapted bR molecule – in its ground state – contains an *all-trans* retinal as the light-sensing chromophore, which is covalently attached to the Lys-216 side chain via a protonated Schiff's base. Upon photon-absorption, the retinal goes to an excited state and isomerizes to its *13-cis* form. After isomerization of the retinal, the protein undergoes a cyclic series of thermally excited conformational changes, while a proton is translocated through the membrane. In the end of

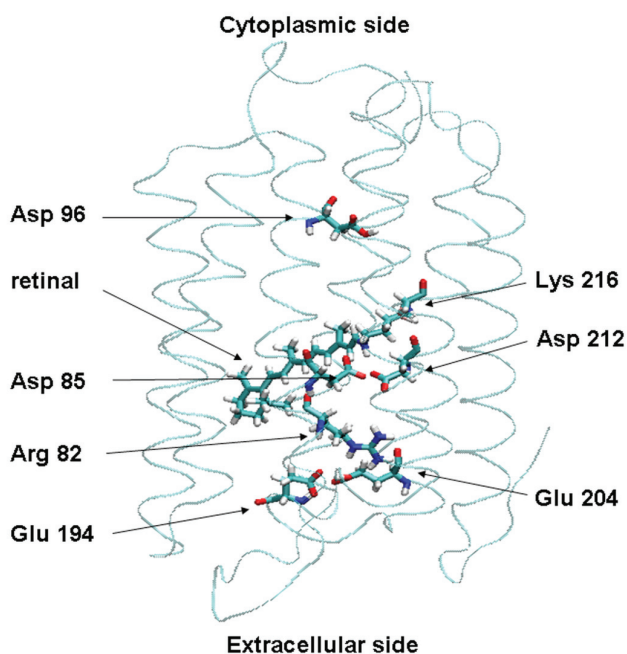


Figure 5. The helical structure of bacteriorhodopsin with some functionally important amino acid residues and the retinal chromophore in the center.

the cycle, the retinal is reprotonated from the cytoplasmic side and the protein relaxes to the ground state. In case of wild-type bacteriorhodopsin (WT bR), the characteristic life time of the whole cycle is about 10 ms. This light-induced proton transport process is called the *photocycle* (Chu Kung et al. 1975; Lozier et al. 1975). During the photocycle, the protein goes through several metastable, spectrally well-distinguishable conformational states, the so called intermediate states (BR_{568} , J_{625} , K_{610} , L_{540} , M_{412} , N_{550} , O_{630}). The lower indices of the intermediate states correspond to their absorption maxima (nm). The time course of intermediate concentrations during the photocycle can be determined by flash-photolysis experiments. After the photocycle is started by a short actinic flash, the relative population of an intermediate state can be followed by absorption spectroscopic methods in the visible range (Kaufmann et al. 1976; Lozier et al. 1976; Dér et al. 1991; Váró and Lanyi 1991; Colonna et al. 2005). The late intermediate states are also photosensitive, the photocycle can be short-cut at any step by applying a second flash exciting the corresponding intermediate state (Ormos et al. 1980). Rate constants of the photocycle in solutions strongly depend on the environmental conditions, e.g., temperature, ionic strength and pH of the solution, buffers.

Structure and function of proteins can be studied by spectroscopic methods ranging from X-rays to terahertz frequencies (Engelhard et al. 1987; Kataoka et al. 1993; Saitō

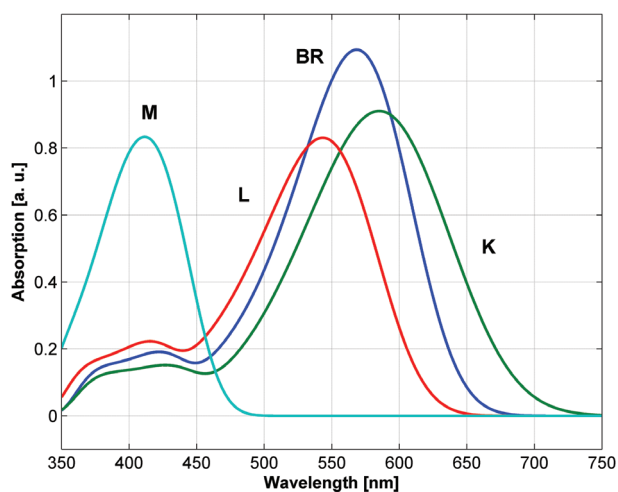


Figure 6. Reconstructed relative absorption spectra of the ground state (BR) and the K, L, M intermediate states of bacteriorhodopsin.

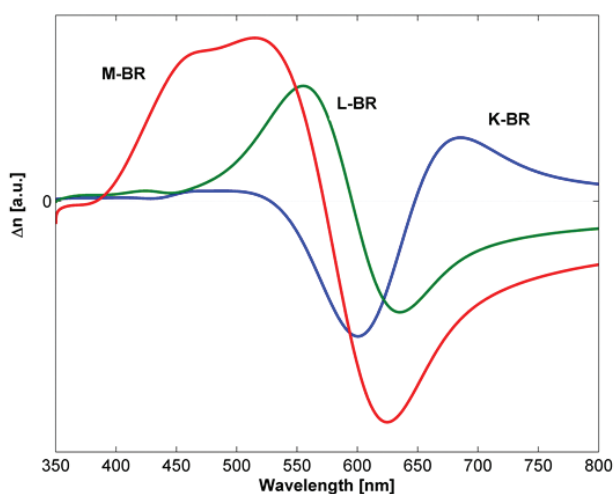


Figure 7. Calculated refractive index changes between some intermediate states (K, L and M) and the ground (BR) state of a dried bacteriorhodopsin layer.

and Naito 2007; Groma et al. 2011). In this work, we deal only with spectroscopic properties in the visible region. The spectra of the intermediate states were determined by several authors using different techniques. Absorption spectra used in this work (Fig. 6) were measured by Gergely et al. (1997) and refined later by Zimányi (2004). Since we want to study the applicability of bacteriorhodopsin as an active optical material in integrated optics, one of the most important properties is the refractive index change between the steps of the photocycle. The absorption difference between two intermediate states also implies a corresponding refractive index change,

according to the Kramers-Kronig relations (Nussenzveig 1972; Wooten 1972). The refractive index changes of the intermediate states with respect to the ground state (BR) have been calculated according to the above Kramers-Kronig relation and are shown in (Fig. 7). As it is expected from the absorption shift, the calculated largest refractive index change is between the BR and M states, approximately -4×10^{-3} at the wavelength of the He-Ne laser (632.8 nm). At the same wavelength, refractive index changes between the BR K and BR L transitions are almost equal, found to be -2×10^{-3} . The calculated refractive index changes are comparable, or even higher than those of organic or inorganic crystals used as active materials in integrated optical devices (Ormos et al. 2002).

In the following section we present proof-of-the-concept experiments using bacteriorhodopsin as active NLO material in ultrafast photonic switching.

Protein-based ultrafast photonic switching

The concept of Tbit/s telecommunication represents the expectations of a serious improvement both in capacity and speed and all-optical (photonic) data processing is considered to be the most promising approach to achieve these goals. Here we present an experimental demonstration of a picosecond photonic switch using the refractive index change of the bR adlayer accompanying the ultrafast BR→K transition, allowing greater than 100 GHz communication speed in integrated optical devices (Fábián et al. 2011).

Earlier experiments concerning the integrated optical applications of bR proved that under continuous illumination, the refractive index of a dried bR-film at 632 nm changes while the M state develops. Consequently, if a probe laser beam at a wavelength outside of the excitation range of bR is coupled into an integrated optical device (e.g., a slab waveguide or a Mach-Zehnder interferometer) covered by an adlayer prepared of bR, the intensity of the output can be modulated by exciting the sample (Ormos et al. 2002; Dér et al. 2007). Optical switching and logical operations based on the BR→M transition were also shown later by other integrated optical structures, as well (Topolancik and Vollmer 2006; Roy et al. 2010; Wolff and Dér 2010). The results of other experiments (Fábián et al. 2011) proved that the BR→K transition can also be utilized in integrated optical applications, suggesting the feasibility of picosecond optical switching, based on the nonlinear optical properties of bacteriorhodopsin.

In order to realize ultrafast photonic switching, pump-probe experiments were carried out on a bR film, using picosecond and femtosecond laser pulses. A short pump pulse at a wavelength in the absorption band of bR ($\lambda=530$ nm) initiated the photocycle of the protein. The light-induced refractive index change was then probed by a subsequent laser pulse at

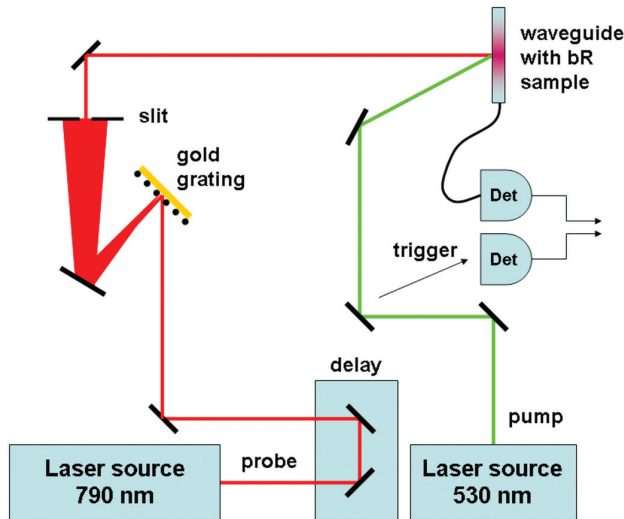


Figure 8. Scheme of the setup used in the ps photonic switch experiments.

a central wavelength around 790 nm, outside the absorption bands of all intermediates, ensuring that the photocycle is unaffected by the probe beam. The investigated transition was characterized by changing the time delay between the pump and probe pulses, as well as their duration. In all experiments pulses generated by a TW-class laser system were used, which provided us with two synchronized pulses centered at 530 nm and 790 nm wavelengths, respectively (Fig. 8). The broadband pulses were generated from the more intense part of the fundamental beam with the unique combination of non-collinear optical parametric chirped pulse amplification (NOPCPA) and chirp-assisted sum-frequency generation (Mero et al. 2011). The less intense part of the beam was used to probe the sample excited by the pump pulse. After an adjustable delay and shaping of their spectral bandwidth the pulses were aimed to the sample, in this case a slab optical waveguide covered by a dried bacteriorhodopsin layer. The outcoupled spectrum and intensity were monitored by a spectrograph and a fast photodiode, respectively. In all of the measurements the incident angle of the probe pulses was tuned to the incoupling range of the TM peak. Due to the refractive index change of the bR adlayer following excitation, the coupling wavelength of a broadband probe pulse is expected to shift, or alternatively, the outcoupled intensity of a narrow-band pulse should change.

The first series of experiments aimed to demonstrate the frequency shift of the incoupled broadband pulse upon excitation of the bR film. A brief conceptual description of the wavelength shift is the following: The incident angle of the probe beam is fixed at the maximum of the incoupling peak

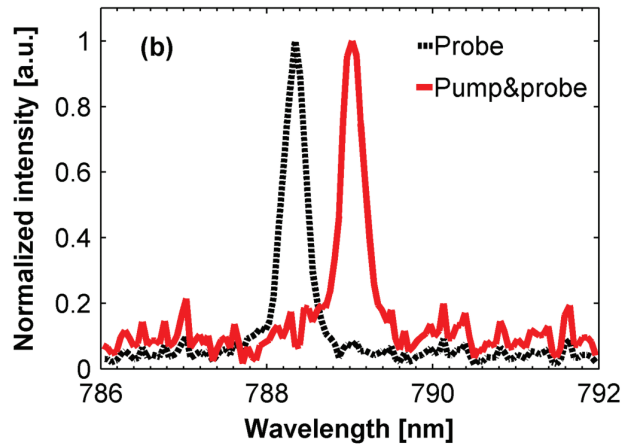


Figure 9. Spectral shift of a broadband probe pulse following the excitation (pump), of the bacteriorhodopsin adlayer.

corresponding to the refractive index (n_A) of the unexcited sample (BR state), determined by the mode equation. In this way we also fix the effective refractive index of the propagating mode (N). Upon excitation, the refractive index of the adlayer changes. Since other parameters of the waveguide have not been changed, the wavelength of the propagating wave should change, in order to fulfill the mode equation with the new value of the adlayer refractive index. Therefore, in case of a broadband probe beam, change in the refractive index of the bR adlayer involves a spectral shift of the outcoupled spectrum that can be measured at the end of the waveguide.

During the measurement, the FWHM (*full-width-at-half-maximum*) bandwidth of the probe pulses of 12 ps was chosen to be 3 nm. The bR photocycle was initiated by the pump pulse with a duration of 45 ps, reaching the sample 100 ps before the probe. Under these conditions, the only intermediate present in the photocycle is the K form, with a red-shifted absorption spectrum relative to the ground (BR) state. As it was demonstrated earlier, such a spectral shift should result in a refractive index increase of the adlayer, when measured at the wavelength of the probe pulse. This refractive index change, in turn, involves a red-shift in the incoupled spectrum, provided that the angle of incidence is unchanged. In fact, traces in (Fig. 9) show a red shift in the spectrum of the incoupled light upon excitation. This type of switching we call “frequency-switching”, because one can select different frequency bands of very narrow bandwidth of a broadband pulse, enabling frequency demultiplexing, an essential operation in optical information processing. According to our calculations based on the mode equations (Tiefenthaler and Lukosz 1989; Ormos et al. 2002; Vörös et al. 2002), the amount of the observed spectral shift corresponds to a refrac-

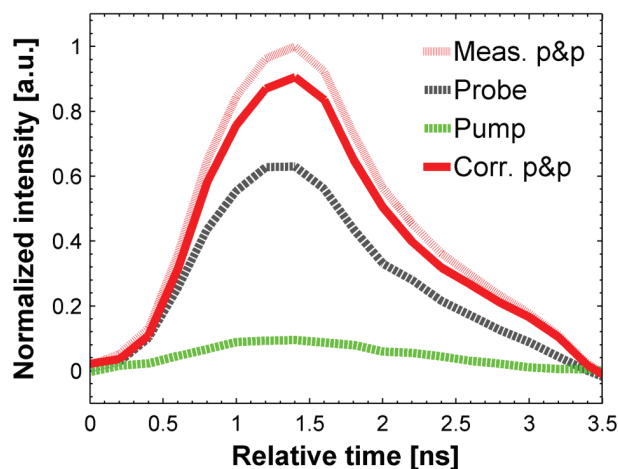


Figure 10. The ps amplitude switching. Time scale reflects only the speed of the detector while that of the optical switching is determined by the BR K transition.

tive index change that is comparable to that observed between BR and M, allowing a direct “amplitude switching”.

We have seen that in the case of a broadband probe pulse, the refractive index change of the adlayer is followed by a spectral shift of the incoupled spectrum, without any change in the intensity. However, if the spectral shift is larger than, or comparable to the half of the FWHM bandwidth of the probe pulse, a decrease in the intensity can be observed, provided the angle of incidence is set to the maximum of the incoupling peak. In order to realize the amplitude switching by the K intermediate, next the bandwidth of the probe pulse was narrowed down to 0.8 nm using a Fabry–Pérot interferometer. The intensity of the outcoupled light was monitored by a fast photodiode. In order to maximize the effect, the angle of incident probe pulse was slightly tuned off the resonance peak, until the output intensity decreased to its half-maximum. As the green pump pulse excites the sample, an angular shift of the incoupling peak occurs and the intensity of the incoupled light increases (Fig. 10).

When both the measuring (probe) and exciting (pump) pulses hit the sample (red line), the incoupled intensity is considerably higher than that when only the probe beam is present (grey dashed line). A small amount of the exciting light is also reached the detector, when the pump beam was on (green line). Correcting to this, the fast intensity modulation achieved in this experiment was about 50%. The above results clearly demonstrate the feasibility of ultrafast all-optical frequency and amplitude switching using the picosecond $BR \rightarrow K$ transition of the bacteriorhodopsin photocycle. More effective switching is expected to be achieved in the future by proper modification of the protein sample (Aharoni et al. 2001) and optimizing the underlying photonic structure.

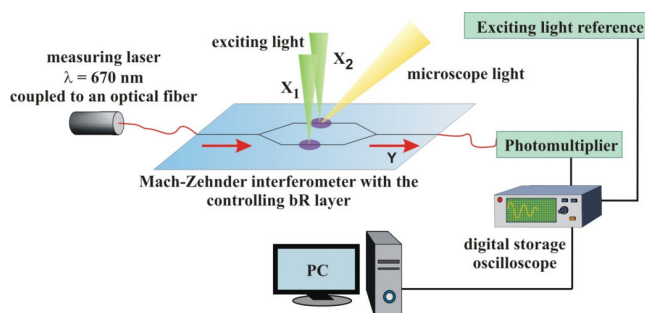


Figure 11. The measuring setup for the bR-based logic gates with the integrated optical Mach-Zehnder interferometer.

Integrated optical logic gates based on bacteriorhodopsin

Having proven the feasibility of bR-based, fast integrated optical switching, bR-based logic gates were planned and realized built around another integrated optical structure, the Mach-Zehnder interferometer (Wolff and Dér 2010; Mathesz et al. 2013). After demonstrating the operation of the gate in different modes (binary and ternary logic) under quasicontinuous illumination conditions, here we show how the gate can perform a high-speed logical operation (as a comparator in ternary logic mode, using nanosecond flashes). Possible implications of the results in integrated photonics are discussed.

In an earlier work (Dér et al. 2007), it was shown that a waveguide-based integrated optical Mach-Zehnder interferometer can act as an all-optical light modulator. The active optical component of the device was made of a dried film of bR layered upon the top of the arms of the interferometer (Fig. 11). Excitation of the bR film by a continuous laser beam shifts the dynamic equilibrium between the concentrations of the ground state (BR_{568}) and the M_{412} intermediate of the bR photocycle, accumulating upon quasi-continuous excitation. (The lower indices refer to the absorption maxima, in nm-s of the corresponding states of the photocycle.) Because of the spectral differences between BR and M, the refractive index of the sample (determined by the ratio of the two states) changes, hence, the effective refractive index of the propagating mode is also altered. When one of the active regions above the interferometer is excited, a phase difference between the two arms develops, consequently, the output intensity changes. Since the ratio of BR and M in the equilibrium mixture depends on the intensity of the continuous-wave excitation, the phase difference between the two arms can be controlled by the exciting light. By a continuous increase of the exciting intensity, a sinusoidal modulation of the output could be observed indicating that, with high enough exciting

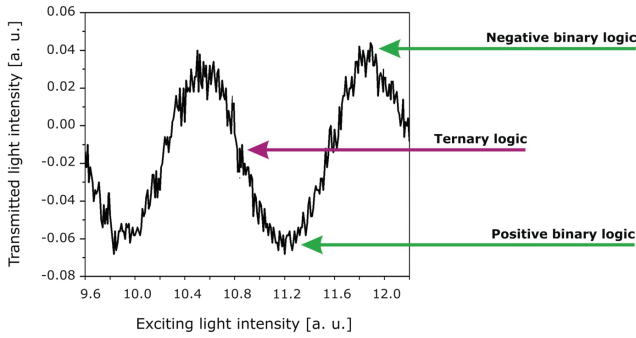


Figure 12. The transmission function of the Mach-Zehnder interferometer.

light, a phase difference higher than 2π can be achieved (Dér et al. 2010).

Setting the operating point (biasing the interferometer)

In order to bias the interferometer on the above grounds, the key step is a proper preadjustment of the phase shift of the light propagating in one arm of the MZ interferometer. This can be realized by changing the refractive index of the bR adlayer on one arm via a CW control illumination (Dér et al. 2010). Depending on its operating point, the MZ could work as a binary (two-state) or ternary (tri-state) logic gate.

If the operating point is set to any of the two extremes of the transmission function, the MZ works as a binary logic gate, while when the operating point is in the middle, the device works as a ternary gate (Fig. 12). Note that the sen-

sitivity of the interferometer, that is proportional to the first derivative of the transmission function for small signals, is considerably higher in the ternary mode.

Since the construction of the above logic device allows both binary and ternary modes of operation, first we demonstrated the feasibility of logic gates in these basic modes with experiments using quasi-continuous illumination both for exciting and measuring light beams. Next, the results of pump-probe experiments will be shown, demonstrating how the device can perform a high-speed logical operation as a ternary-logic comparator, using nanosecond laser flashes.

Binary mode

As it was described in the previous section, the input values of our logic device were provided by the quasi-continuous exciting laser beams, while the output was defined by the intensity level of the outcoupled measuring light. For the input values, the presence of excitation corresponds to logic 1, while the absence of it to logic 0. At the output, logic 1 is represented by high output light intensity of the interferometer, while logic 0 by low one.

Inverter

The first test of the device is carried out on an inverter (or a NOT gate), the simplest logic gate. The input value (X_2) was changed for certain time intervals from 0 to 1, and, as output values, 1 and 0 were got, accordingly. Figure 13A shows the corresponding experimental data.

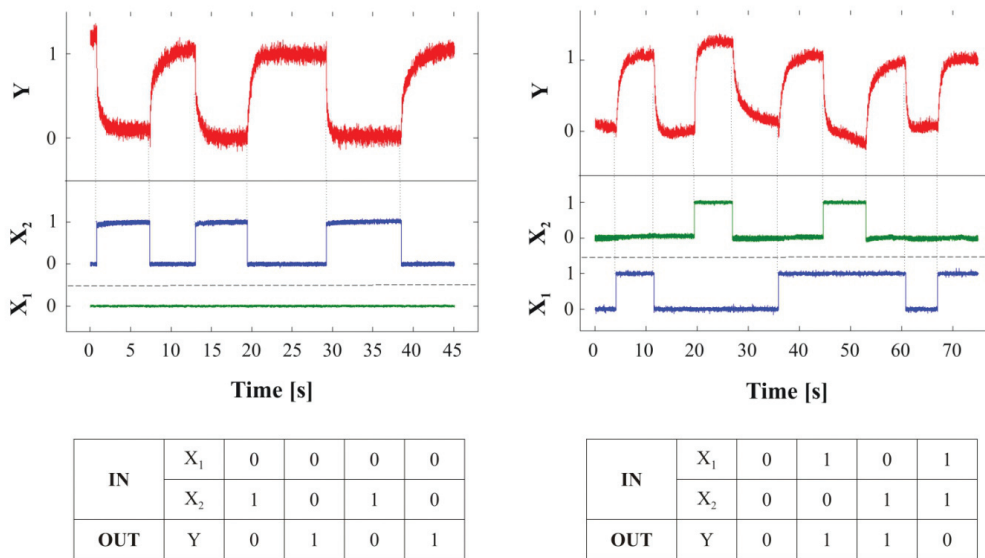


Figure 13. The realization of binary inverter (A) and XOR (B) gates, and their truth tables.

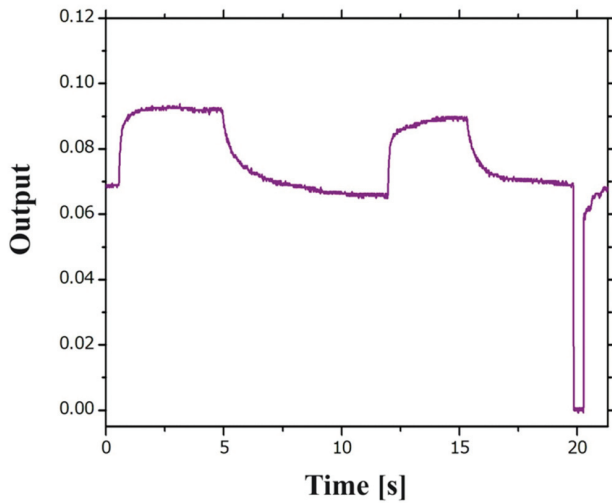


Figure 14. Demonstration of bR-based switching at a telecom wavelength (1350 nm). Intensity changes at the output of the Mach-Zehnder interferometer were measured upon rectangular exciting pulses of 532nm (not shown).

XOR

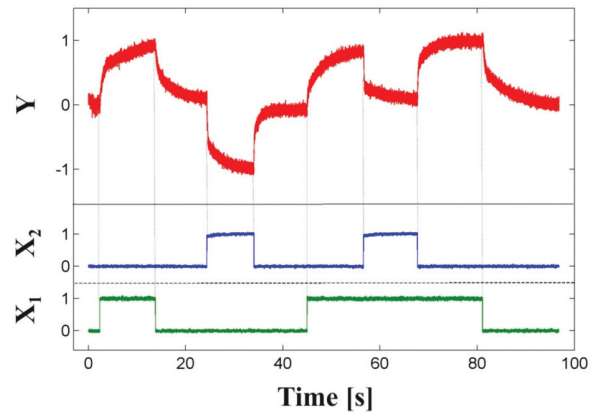
As a next step, an XOR gate was realized with the Mach-Zehnder device. First, the operating point of the interferometer was adjusted to a minimum of the transmission function to achieve a binary gate. Afterwards, the branches were excited alternatively or simultaneously. The results and the corresponding truth table of the XOR gate are shown in Figure 13B.

The above results demonstrate that a bR-based integrated optical device can properly function in the form of various types of logic gates in the binary mode, as was predicted in (Wolff and Dér 2010). Since the most widespread applications of photonic switching are related to the telecommunication industry, it was important to demonstrate that the NLO properties of bR allow optical switching also in the telecom wavelength regime (Fig. 14).

In the following, we focus on the ternary mode of operation, where the higher sensitivity of the device allows lower input light levels, and faster response times.

Ternary mode

Although, at the dawn of machine computing, ternary logic was considered to be a favourable choice (Glusker et al. 2005), the only modern, electronic ternary computer (Setun) was built in the late 1950, and a newer version in the 1970s (Hunger 2008). Nowadays, the idea of ternary computing is being revisited, because of its theoretical advantages over binary logic (Connelly 2008). Given a set of assumptions outlined in (Hayes 2001), base *e* is the most efficient



IN	X ₁	0	1	0	1
	X ₂	0	0	1	1
OUT	Y	0	1	-1	0

Figure 15. Experimental data and truth table of the all-optical comparator realized as a ternary logic gate.

base for representing arbitrary numbers. Since in practice the base must be an integer, ternary logic would be more efficient than binary (Hurst 1984; Dhande and Ingole 2005). In fact, its advantages have been confirmed in digital memories, communications components, and the field of digital signal processing (Wu and Huang 1993). Despite, the practical realization of ternary computing has still been considered to be a matter of debate (Connelly 2008).

As a simple but important device working in the ternary logic mode, an integrated optical comparator was realized. In electronics, a comparator is a device that compares two input signals, and indicates at the output, which one is larger. It is easy to see that if the operating point is set to the middle of the sinusoidal transmission function curve (Fig. 12), the IO device can perform the function of an all-optical comparator. Excitation of each arm leads to phase difference changes with opposite signs, therefore the output intensity changes oppositely in the two cases. Moreover, collective excitation of the arms leads to zero phase change when the output remains unchanged.

In one series of experiments, quasi-continuous illumination was used for the input signals. In Figure 15, it is shown, that the output light intensity level changes in the opposite direction when alternatively exciting the bR films above the two arms of the interferometer. If, namely, $X_1 > X_2$, the output signal is positive, while if $X_1 < X_2$, it is negative. If the input values are equal ($X_1 = X_2$), the output intensity does not change. Note that the input intensities applied in this case

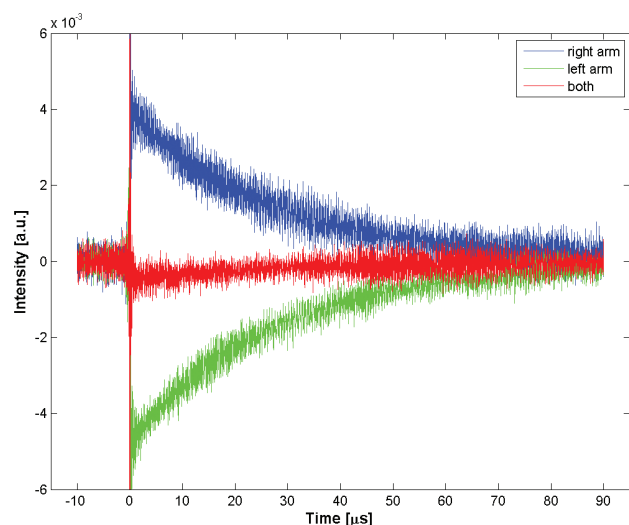


Figure 16. Demonstration of the fast operation mode of the comparator.

were ca. 3 times smaller than those used during the experiments in the binary mode.

In another set of experiments, another advantage of the ternary-mode-device was utilized, namely that the high sensitivity of the MZ device at the ternary working point allows to demonstrate a high-speed operation. The optical path difference between the pump and probe beams was carefully adjusted so that they hit the sample at the same time. Intensity change traces measured at the output of the MZI in the case of distinct (blue or green, respectively) and collective (red curve) excitation of the arms of the MZI are shown on Figure 16. Note that, though, the kinetics of the recorded traces were limited by the relaxation time of the electronic detection system (ca. 20 μs), the time resolution of the optical logical device is determined by the ns time course of the pump and probe pulses, as usual in pump-probe experiments. Taking into account the linear response of the interferometer and the picosecond rise time of the K intermediate, in this case, the speed of the switch is limited by the pulse length of the pump and probe beams.

Conclusions

The above examples convey, that bacteriorhodopsin can easily find applications in waveguide-based integrated optical devices, as an active NLO material. The amount and speed of refractive index changes accompanying the photocycle are comparable to, or even higher than those of the inorganic crystals recently used. Its stability, fast, light-induced, geneti-

cally tailorable photochemical reactions and favorable nonlinear optical properties make it a promising candidate in future integrated optical devices. The efficiency of the biophotonic switching is expected to be enhanced further by optimizing the underlying integrated optical structures.

Acknowledgement

The authors are grateful to Profs. Pál Ormos, J.J. Ramsden and E.K. Wolff for their contribution to the scientific results presented in this review. This work was supported by the TÁMOP-4.1.1.C-13/1/KONV-2014-0001 program entitled „Practice-oriented, student-friendly modernization of the biomedical education for strengthening the international competitiveness of the rural Hungarian universities”.

References

- Aharoni A, Hou B, Friedman N, Ottolenghi M, Rousso I, Ruhman S, Sheves M, Ye T, Zhong Q (2001) Non-isomerizable artificial pigments: Implications for the primary light-induced events in bacteriorhodopsin. *Biochemistry-Moscow* 66:1210-1219.
- Bogomolni RA, Baker RA, Lozier RH, Stoekenius W (1976) Light-driven proton translocations in *Halobacterium halobium*. *Biochim Biophys Acta* 440:68-88.
- Chu Kung M, DeVault D, Hess B, Oesterhelt D (1975) Photolysis of bacterial rhodopsin. *Biophys J* 15:907-911.
- Colonna A, Groma GI, Vos MH (2005) Retinal isomerization dynamics in dry bacteriorhodopsin films. *Chem Phys Lett* 415:69-73.
- Connelly J (2008) “Ternary Computing Testbed: 3-trit Computer Architecture.” California Polytechnic State University.
- Dér A, Száraz S, Tóth-Boconádi R, Tokaji Z, Keszthelyi L, Stoekenius W (1991) Alternative translocation of protons and halide-ions by bacteriorhodopsin. *PNAS* 88:4751-4755.
- Dér A, Tóth-Boconádi R, Keszthelyi L, Kramer H, Stoekenius W (1995) Orientation of purple membrane in combined electric and magnetic fields. *FEBS Lett* 377:419-420.
- Dér A, Valkai S, Fábián L, Ormos P, Ramsden JJ, Wolff EK (2007) Integrated optical switching based on the protein bacteriorhodopsin. *Photochem Photobiol* 83:393-396.
- Dér A, Valkai S, Mathesz A, Andó I, Wolff EK, Ormos P (2010) Protein-based all-optical sensor device. *Sensors and Actuators B: Chemical* 151:26-29.
- Dhande A, Ingole V (2005) “Design and implementation of 2 bit ternary ALU slice.” In *Proc Int Conf IEEE-Sci Elec*

- tron, Technol Inf Telecommun, 17-21, Tunisia.
- Engelhard M, Hess B, Chance M, Chance B (1987) X-ray absorption studies on bacteriorhodopsin. *FEBS Lett* 222:275-278.
- Fábián L, Heiner Z, Mero M, Kiss M, Wolff EK, Ormos P, Osvay K, Dér A (2011) Protein-based ultrafast photonic switching. *Opt Expr* 19:18861-18870.
- Fischer T, Neebe M, Juchem T, Hampp NA (2003) Biomolecular optical data storage and data encryption. *IEEE Trans Nanobiosci* 2:1-5.
- Gergely C, Zimányi L, Váró G (1997) Bacteriorhodopsin intermediate spectra determined over a wide pH range. *J Phys Chem B* 101:9390-9395.
- Glusker M, Hogan DM, Vass P (2005) The ternary calculating machine of Thomas Fowler. *IEEE Ann Hist Comput* 27:4-22.
- Groma GI, Colonna A, Martin J-L, Vos MH (2011) Vibrational motions associated with primary processes in bacteriorhodopsin studied by coherent infrared emission spectroscopy. *Biophys J* 100:1578-1586.
- Hales JM, Matichak J, Barlow S, Ohira S, Yesudas K, Bredas J-L, Perry JW, Marder RR (2010) Design of polymethine dyes with large third-order optical nonlinearities and loss figures of merit. *Science* 327:1485-1487.
- Haque SA, Nelson J (2010) Toward organic all-optical switching. *Science* 327:1466-1467.
- Hartmann R, Sickinger H-D, Oesterhelt D (1977) Quantitative aspects of energy conversion in halobacteria. *FEBS Lett* 82:1-6.
- Hayes B (2001) Third Base. *Am Sci* 89:490.
- Henderson R, Baldwin JM, Downing KH, Lepault J, Zemlin F (1986) Structure of purple membrane from *Halobacterium halobium*: recording, measurement and evaluation of electron micrographs at 3.5 Å resolution. *Ultramicroscopy* 19:147-178.
- Henderson R, Shotton D (1980) Crystallization of purple membrane in three dimensions. *J Mol Biol* 139:99-109.
- Hu X, Jiang P, Ding C, Yang H, Gong Q (2008) Picosecond and low-power all-optical switching based on an organic photonic bandgap microcavity. *Nat Phot* 2:185-189.
- Hunger F (2008) SETUN. An Inquiry into the Soviet Ternary Computer. Leipzig: Institut für Buchkunst.
- Hurst SL (1984) Multiple-valued logic - its status and its future. *IEEE Trans Computers* C-33:1160-1179.
- Kataoka M, Mihara K, Kamikubo H, Needleman R, Lanyi JK, Tokunaga F (1993) Trimeric mutant bacteriorhodopsin, D85N, shows a monophasic CD spectrum. *FEBS Lett* 333:111-113.
- Kaufmann KJ, Rentzepis PM, Stoeckenius W, Lewis A (1976) Primary photochemical processes in bacteriorhodopsin. *Biochem Biophys Res Comm* 68:1109-1115.
- Lozier RH, Bogomolni RA, Stoeckenius W (1975) Bacteriorhodopsin - light-driven proton pump in *Halobacterium halobium*. *Biophys J* 15:955-962.
- Lozier RH, Niederberger W, Bogomolni RA, Hwang S, Stoeckenius W (1976) Kinetics and stoichiometry of light-induced proton release and uptake from purple membrane fragments, *Halobacterium halobium* cell envelopes, and phospholipid vesicles containing oriented purple membrane. *Biochim Biophys Acta* 440:545-556.
- Mathesz A, Fábián L, Valkai S, Alexandre D, Marques PVS, Ormos P, Wolff EK, Dér A (2013) High-speed integrated optical logic based on the protein bacteriorhodopsin. *Biosens Bioelectron* 46:48-52.
- Mero M, Sipos A, Kurdi G, Osvay K (2011) Generation of energetic femtosecond green pulses based on an OPCPA-SFG scheme. *Opt Expr* 19:9646-9655.
- Moore GE (1965) Cramming more components onto integrated circuits. *Electronics* 38:114-117.
- Nussenzweig HM (1972) Casualty and Dispersion Relations. Vol. 95 Mathematics in Science and Engineering, Bellmann R, ed., Academic Press, New York.
- Oesterhelt D, Stoeckenius W (1971) Rhodopsin-like protein from purple membrane of *Halobacterium halobium*. *Nat New Biol* 233:149-152.
- Oesterhelt D, Stoeckenius W (1973) Functions of a new photoreceptor membrane. *PNAS* 70:2853-2857.
- Ormos P, Dancsházy Z, Keszthelyi L (1980) Electric response of a back photoreaction in the bacteriorhodopsin photocycle. *Biophys J* 31:207-213.
- Ormos P, Fábián L, Oroszi L, Ramsden JJ, Wolff EK, Dér A (2002) Protein-based integrated optical switching and modulation. *Appl Phys Lett* 80:4060-4062.
- Ovchinnikov YA, Abdulaev NG, Feigina MY, Kiselev AV, Lobanov NA (1979) The structural basis of the functioning of bacteriorhodopsin: An overview. *FEBS Lett* 100:219-224.
- Roy S, Prasad M, Topolancik J, Vollmer F (2010) All-optical switching with bacteriorhodopsin protein coated microcavities and its application to low power computing circuits. *J Appl Phys* 107:053115.
- Saitō H, Naito A (2007) NMR studies on fully hydrated membrane proteins, with emphasis on bacteriorhodopsin as a typical and prototype membrane protein. *Biochim Biophys Acta* 1768:3145-3161.
- Service RF (1995) Two steps for light-altering polymers. *Science* 268:1570.
- Song QW, Zhang C, Gross RB, Birge RR (1994) The intensity-dependent refractive index of chemically enhanced bacteriorhodopsin. *Opt Comm* 112:296-301.
- Stoeckenius W (1985) The rhodopsin-like pigments of halobacteria: light-energy and signal transducers in an archaebacterium. *Trends Biochem Sci* 10:483-486.
- Stuart JA, Marcy DL, Birge RR (2001) Photonic and optoelectronic application of bacteriorhodopsin In *Bioelectronic Applications of Photochromic Pigments*, eds., Dér

- A and Keszthelyi L, pp. 15-29.
- Stuart JA, Marcy DL, Wise KJ, Birge RR (2002) Volumetric optical memory based on bacteriorhodopsin. *Synthetic Met* 127:3-15.
- Thoma R, Hampp N (1994) Adaptive bacteriorhodopsin-based holographic correlator for speed measurement of randomly moving three-dimensional objects. *Opt Lett* 19:1364-1366.
- Tiefenthaler K, Lukosz W (1989) Sensitivity of grating couplers as integrated optical chemical sensors. *JOSA B Opt Phys* 6:209-220.
- Topolancik J, Vollmer F (2006) All-optical switching in the near infrared with bacteriorhodopsin-coated microcavities. *Appl Phys Lett* 89:184103.
- Váró G, Lanyi JK (1991) Distortions in the photocycle of bacteriorhodopsin at moderate dehydration. *Biophys J* 59:313-322.
- Vörös J, Ramsden JJ, Csúcs G, Szendrő I, De Paul SM, Textor M, Spencer ND (2002) Optical grating coupler biosensors. *Biomaterials* 23:3699-3710.
- Vsevolodov N (1998) *Biomolecular electronics*. Boston: Birkhauser.
- Wolff EK, Dér A (2010) All-optical logic. *Nanotech Percept* 6:51-56.
- Wooten F (1972) *Optical Properties of Solids*. New York: Academic Press.
- Wu C-Y, Huang H-Y (1993) Design and application of pipelined dynamic CMOS ternary logic and simple ternary differential logic. *IEEE J Solid-St Circ* 28:895-906.
- Zhang YH, Wang Song Q, Tseronis C, Birge RR (1995) Real-time holographic imaging with a bacteriorhodopsin film. *Opt Lett* 20:2429-2431.
- Zimányi L (2004) Analysis of the bacteriorhodopsin photocycle by singular value decomposition with self-modeling: a critical evaluation using realistic simulated data. *J Phys Chem B* 108:4199.